TOMOGRAPHY® RESEARCH ARTICLE

Longitudinal Measurements of Intra- and Extracellular pH Gradient in a Rat Model of Glioma

Heeseung Lim[1], Mohammed Albatany[1], Francisco Martínez-Santiesteban[1], Robert Bartha[1,2], and Timothy J. Scholl[1,2,3]

[1]Department of Medical Biophysics, University of Western Ontario, London, ON, Canada, [2]Robarts Research Institute, University of Western Ontario, London, ON, Canada, and [3]Ontario Institute for Cancer Research, Toronto, ON, Canada

Corresponding Author:
Timothy J. Scholl, PhD
1151 Richmond St. N., London, ON, Canada N6A 5B7;
E-mail: scholl@uwo.ca

Key Words: pH mapping, pH gradient, CEST, hyperpolarized ^{13}C bicarbonate, glioma
Abbreviations: Chemical exchange saturation transfer (CEST), magnetic resonance imaging (MRI), amine and amide concentration-independent detection (AACID), magnetic resonance spectroscopic imaging (MRSI), fast spin-echo pulse sequence (FSE), field of view (FOV), repetition time (TR), echo time (TE), echo train length (ETL), radiofrequency (RF), water saturation shift referencing (WASSR), regions of interest (ROIs)

ABSTRACT

This study presents the first longitudinal measurement of the intracellular/extracellular pH gradient in a rat glioma model using noninvasive magnetic resonance imaging. The acid–base balance in the brain is tightly controlled by endogenous buffers. Tumors often express a positive pH gradient ($pH_i - pH_e$) compared with normal tissue that expresses a negative gradient. Alkaline pH_i in tumor cells increases activity of several enzymes that drive cellular proliferation. In contrast, acidic pH_e is established because of increased lactic acid production and subsequent active transport of protons out of the cell. pH_i was mapped using chemical exchange saturation transfer, whereas regional pH_e was determined using hyperpolarized ^{13}C bicarbonate magnetic resonance spectroscopic imaging. pH_i and pH_e were measured at days 8, 12, and 15 postimplantation of C6 glioma cells into rat brains. Measurements were made in tumors and compared to brain tissue without tumor. Overall, average pH gradient in the tumor changed from -0.02 ± 0.12 to 0.10 ± 0.21 and then 0.19 ± 0.16. Conversely, the pH gradient of contralateral brain tissue changed from -0.45 ± 0.16 to -0.25 ± 0.21 and then -0.34 ± 0.25 (average pH $\pm$ 1 SD) Spatial heterogeneity of tumor pH gradient was apparent at later time points and may be useful to predict local areas of treatment resistance. Overall, the intracellular/extracellular pH gradients in this rat glioma model were noninvasively measured to a precision of ~0.1 pH units at 3 time points. Because most therapeutic agents are weak acids or bases, *a priori* knowledge of the pH gradient may help guide choice of therapeutic agent for precision medicine.

INTRODUCTION

Cancer is a physiologically and genetically diverse disease, resulting in abnormal cellular proliferation. Cancer cells have altered biological pathways and microenvironment that support this proliferation. These changes have been widely studied and some categorized as *hallmark* features of cancer because they are common to many types of genetically diverse tumors (1) and affect important aspects of cancer progression and therapy. Among the identified hallmarks, deregulation of metabolism and poor vascularization are main contributors to altered intra- and extracellular pH within tumors (1-4). Altered tumor pH, in particular the intracellular-to-extracellular pH gradient, is an important factor that drives cancer progression, by enhancing oncogene expression, increasing metastatic potential, and altering drug efficacy (5-8).

Cellular pH gradient is defined as the difference between intracellular pH (pH_i) and extracellular pH (pH_e). In normal tissue, pH_i is ~7.2 and pH_e is ~7.4 (7, 9, 10), resulting in a negative pH gradient (approximately −0.2) across the cellular membrane. In contrast, tumor cells possess a positive pH gradient (~0.5), where pH_i is ~7.4 and pH_e is ~6.9 (7-9, 11, 12). This reversal of the pH gradient is the result of modified cellular metabolism, which promotes tumor cell growth and invasion. Most cancer cells rely on aerobic glycolysis [Warburg effect (13, 14)] to generate energy for cellular function. This results in increased production of protons and lactate and would lead to a reduction in intracellular pH (4), which would normally damage a cell. However, tumor cells actively maintain homeostasis by transporting protons and lactate into the extracellular space (15). Inefficient tumor vasculature cannot support the bicarbonate/

ISSN 2379-1381 http://dx.doi.org/10.18383/j.tom.2018.00001

carbon dioxide buffer system, so the extracellular space of tumor becomes more acidic (15). This leads to the destruction of the extracellular matrix, promoting tumor cell invasion and eventually metastasis (7). Furthermore, excretion of excess carbon as lactate may be an effective means of incorporating carbon into biomass, supporting increased cellular proliferation (16).

Several noninvasive imaging techniques have been developed to quantify intra- and extracellular tissue pH (11). In this study, intracellular tissue pH was measured using a novel chemical exchange saturation transfer (CEST) magnetic resonance imaging (MRI) technique called amine and amide concentration-independent detection (AACID) (17). This method exploits the differential pH dependence of the exchange rate of amine and amide protons with bulk water to measure pH. A CEST image is produced to determine the ratio of the amine-to-amine CEST effect, which can be converted into the measurement of intracellular pH from a separate calibration (17). Extracellular tissue pH was measured with hyperpolarized ^{13}C magnetic resonance spectroscopic imaging (MRSI). The use of ^{13}C-labelled bicarbonate as a contrast agent to evaluate pH_e was previously reported in the literature (18). Hyperpolarized ^{13}C bicarbonate is injected into the vasculature, and after circulation, it reaches the tissue of interest where it exchanges with the pre-existing bicarbonate/carbon dioxide pool under carbonic anhydrase activity. Extracellular pH can be derived from the Henderson–Hasselbalch equation using the ratio of ^{13}C bicarbonate and (13) CO_2 measured by ^{13}C MRSI. By serially combining these approaches, the pH gradient of tissue can be mapped and quantified in the same preclinical model.

This study followed the progression of the pH gradient of tumor cells in an untreated orthotopic rodent model of glioma. C6 rat glioma tumors exhibit rapid growth, vascularization, and invasion (19). Previous studies have noted that these tumors develop necrotic cores and exhibit regional hypoxia (19, 20). Adequate vascularization facilitates effective delivery of hyperpolarized ^{13}C bicarbonate to the tumor. For such an aggressive tumor model, significant changes in the pH gradient are expected over time, making it an ideal solid tumor model for longitudinal studies of tumor pH.

The purpose of this study was to measure and characterize longitudinal changes in the tumor pH gradient. Several studies have measured pH of tissue using techniques described above (17, 18, 21-23). However, no longitudinal study has measured both pH_e and pH_i consecutively to map regional differences and temporal changes in pH gradient in an untreated tumor. We hypothesized that the pH gradient would increase over time as the tumor increases in size. Having knowledge of pH gradient and selecting appropriate therapy are vital for tumor characterization, as the outcome of therapy can be dependent on pH. The results of this study provide insight regarding changes in tumor pH linked to aggressive growth.

METHODOLOGY

^{13}C Bicarbonate Sample Preparation

^{13}C cesium bicarbonate (95% enriched; Sigma Aldrich, Miamisburg, OH) was dissolved in a 4:1 glycerol and deuterium oxide mixture at a final concentration of 6.3 mol/L. In addition, OX63 trityl radical (Oxford Instruments, Concord, MA) and ProHance gadolinium contrast agent (Bracco Diagnostics, Monroe Township, NJ) were added to the sample at final concentrations of 25 mmol/L and 0.5 mol/L, respectively. The final mixture was heated to 60°C and stirred to dissolve. The resulting bicarbonate preparation was stored at −4°C for later use.

Hyperpolarization

^{13}C cesium bicarbonate was hyperpolarized using dynamic nuclear polarization (HyperSense, Oxford Instruments, Abingdon, UK). The bicarbonate sample was cooled to 1.4 K at 3.3 T in the dynamic nuclear polarization apparatus and irradiated with 50 mW of microwave radiation at a frequency of 94.123 GHz to transfer electronic spin magnetization to the ^{13}C-labeled bicarbonate. Approximately 90% solid-state polarization was achieved during 2 h of hyperpolarization. The sample was rapidly mixed with a superheated mixture of 80-mmol/L phosphate buffer (pH = 7.2) and 100-mg/L ethylenediamine tetraacetic acid disodium salt dehydrate (Sigma-Aldrich, St. Louis MO). The resulting hyperpolarized solution had a ^{13}C bicarbonate concentration of 150 mmol/L and a pH of 7.4 at 37°C. The in vitro spin lattice relaxation time and polarization values of the ^{13}C nucleus were 26.2 ± 1.4 s and ~7.5% measured at 3 T (24).

Animal Model

In total, seven Wistar rats weighing ~250 g (~5- to 7-week-old) were used in this study. On day 0, the right caudate nuclei of these rats were surgically implanted with a 10-μL suspension containing ~1 million C6 rat glioma cells. Animals were scanned on days 8, 12, and 15. CEST was performed first using a 9.4-T small animal MRI scanner (Agilent, Santa Clara, CA) to measure pH_i. Under anesthesia, the animals were then transferred to a 3 T MRI for hyperpolarized ^{13}C MRSI to determine pH_e. All animal procedures were performed in accordance with relevant guidelines and regulations stipulated by an animal use protocol approved by the University Council on Animal Care, Animal Use Subcommittee at Western University.

Chemical Exchange Shift Imaging for Intracellular pH

CEST imaging on the 9.4 T MRI was performed with a 50-mm-diameter volume birdcage coil built in-house. Standard anatomical T2-weighted images were used for tumor localization. The T2-weighted images were acquired using a 2D fast spin-echo pulse sequence (FSE) with the following parameters: field of view (FOV) = 38.4 × 38.4 mm^2, isotropic in-plane resolution = 0.3 mm, section thickness = 1 mm, repetition time (TR) = 3000 milliseconds, echo time (TE) = 10 milliseconds, echo train length (ETL) = 4, and effective TE = 40 milliseconds. Upon initial tumor detection by MRI, 2 sections from the T2-weighted image data with maximum tumor extent were selected for CEST imaging. Three sequential CEST images were acquired using an FSE sequence with the following parameters: FOV = 38.4 × 38.4 mm^2, in-plane resolution = 0.6 mm, section thickness = 2 mm, TR = 7000 milliseconds, TE = 7 milliseconds, ETL = 32, and effective TE = 7 milliseconds, preceded by a continuous radiofrequency (RF) pulse with an amplitude of 1.5 μT and a duration of 4 seconds. CEST images were acquired at different saturation frequencies (1.2 to 4.5 [Δ = 0.1] ppm, from 5.4 to 6.6 [Δ = 0.1] ppm, −1000- and 1000-ppm images were acquired as

reference, producing a total of 49 images). For B_0 correction, a water saturation shift referencing (WASSR) technique was used (25). A linearly spaced 37-point WASSR CEST spectrum with saturation frequencies from −0.6 to 0.6 ppm was acquired using the same pulse sequence except preceded by a shorter-duration RF saturation pulse (100 milliseconds) with low amplitude (0.2 μT). Each WASSR spectrum and CEST spectrum was interpolated to achieve 1-Hz resolution. Each CEST spectrum was then frequency-shifted, using the corresponding WASSR spectrum, to account for B_0 variation. B_0 variations were corrected on a pixel-by-pixel basis. The three CEST spectra were summed for each pixel following B_0 corrections to increase signal-to-noise ratio. A B_1 field map was generated using a flip angle imaging pulse sequence (TR = 20 milliseconds, TE = 3.47 milliseconds, echoes = 2, flip angle = 700, FOV = 38.4 × 38.4 mm^2, matrix size = 64 × 64). Observed B_1 variations in the CEST section were <5%, and no B_1 correction was applied.

Hyperpolarized ^{13}C Bicarbonate MRSI for Extracellular pH

A switch-tuned ^{1}H–^{13}C RF coil was used to acquire inherently coregistered proton images and ^{13}C MRSI data of the rat models at 3 T (26). Tumors were identified using a T2-weighted anatomical ^{1}H scan of the rat brain using an FSE sequence with the following parameters: FOV = 80.0 × 80.0 mm^2, isotropic in-plane resolution = 0.3 mm, section thickness = 3 mm, TR = 4000 milliseconds, TE = 85 milliseconds, bandwidth = 10.42 kHz, ETL = 16, and number of averages = 4. Before hyperpolarized ^{13}C imaging, rats were injected with 3 mL of buffered hyperpolarized ^{13}C bicarbonate solution in a single 12-second bolus through a tail vein catheter. Dynamic ^{13}C maps of bicarbonate and carbon dioxide were collected using a spectral–spatial excitation chemical shift imaging sequence [FIDALL (27)] with the following parameters: frequency excitations (bicarbonate and CO_2, 35.5 ppm difference) = 2, FOV = 60.0 × 60.0 mm^2, isotropic in-plane resolution = 3.5 mm, section thickness = ~12 mm, TR = 350 milliseconds, and flip angle for bicarbonate/CO_2 excitation = 5°/90°.

Hyperpolarized ^{13}C Bicarbonate MRSI for Extracellular pH Calibration

To calibrate pH measurement from hyperpolarized ^{13}C bicarbonate, 4 separate phosphate buffers with different pH values (6.4, 6.6, 6.8, 7.0) were prepared before the experiments. Further, 1 mm of each phosphate buffer was mixed with an equal volume of 200-mmol/L buffered hyperpolarized ^{13}C bicarbonate solution. For catalysis, 1 mg of carbonic anhydrase (Sigma Aldrich, Miamisburg, OH), corresponding to ~2500 Wilbur–Anderson units, was added to each solution as a catalyst. The resulting mixtures were imaged with MRSI at 3 T (General Electric Healthcare Discovery MR750 3.0 T, Milwaukee, WI). Immediately after imaging, the pH of each mixture was recorded using a pH meter (VWR Symphony SB70P digital bench-model pH meter, VWR International, Mississauga, ON, Canada). The pH_e image and the correlation between observed and measured pH_e are shown in Figure 1.

Data Analysis

Data analysis of the CEST and hyperpolarized ^{13}C bicarbonate MRSI was performed using MATLAB (MathWorks Inc., Natick, MA). Using B_0-corrected and smoothed CEST spectra, AACID values were measured on a voxel-by-voxel basis. AACID data represent the ratio of the CEST effects of amine protons resonating at 2.75 ppm and amide protons at 3.50 ppm, normalized by magnetization transfer effects measured after saturation at 6.0 ppm and are calculated using the following equation from McVicar et al. (17):

$$\text{AACID} = \frac{M_z(3.50ppm) \times (M_z(6.00ppm) - M_z(2.75ppm))}{M_z(2.75ppm) \times (M_z(6.00ppm) - M_z(3.50ppm))} \quad (1)$$

Here, $M_z(f)$ is the magnitude of the CEST signal at a specific frequency, f. AACID is linearly dependent on pH_i and is insensitive to change in T1 relaxation time, temperature, and macromolecule concentration (17). We calibrated the relationship between AACID and pH in both tumor and contralateral brain regions of interest (ROIs). For hyperpolarized ^{13}C bicarbonate MRSI, non-Cartesian k-space data were reconstructed into maps of ^{13}C-bicarbonate and ^{13}C-carbon dioxide (28). Regional pH_e was calculated using the following Henderson–Hasselbalch equation (29):

$$pH_e = pk_a + \log_{10}\frac{[HCO_3^-]}{[CO_2]} \quad (2)$$

Here, pH_e is the extracellular pH, pk_a (6.17) (29) is the base-10 logarithm of the acid dissociation constant of carbonic acid, and $[HCO_3^-]$ and $[CO_2]$ are the concentrations of bicarbonate and carbon dioxide, respectively. The bicarbonate-to-carbon dioxide concentration ratio is determined as the ratio of MRSI signal amplitudes of ^{13}C-bicarbonate and ^{13}C-carbon dioxide after corrections for individual flip angle excitations.

Statistics

ROIs for tumor and contralateral brain tissues were manually segmented on both 3 T and 9.4 T T2-weighted images using ITK-Snap [www.itksnap.org, (30)] before image registration. Tumor volumes were measured from observer-drawn ROIs and interobserver variability was used for all volume errors. (Inter-

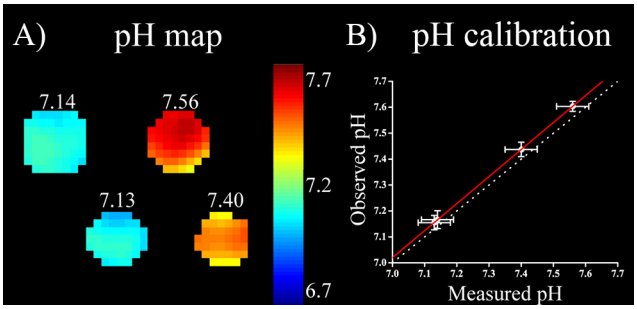

Figure 1. Calibration data for different pH-buffered solutions mixed with hyperpolarized ^{13}C bicarbonate. A pH map derived from ^{13}C magnetic resonance spectroscopic imaging (MRSI) and the corresponding pH values obtained by pH meter (A). The linear regression between measured pH (pH meter) and observed pH (hyperpolarized ^{13}C bicarbonate) with R^2 = 1 (B).

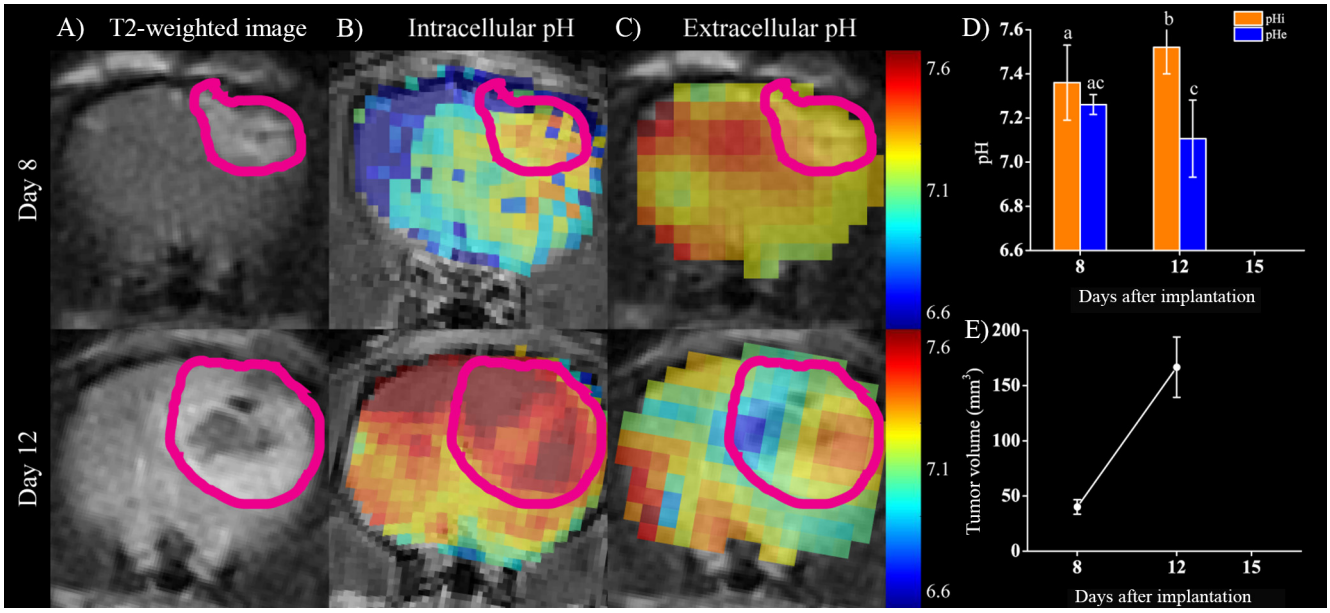

Figure 2. The progression of intra- and extracellular pH of a representative C6 glioma. Panels (A) (B) and (C) present the T2-weighted images, intracellular pH map, and extracellular pH maps of the rat brain, respectively, at days 8 and 12. Tumors are contoured in magenta. Quantification of changes of intra- and extracellular tumor pH (D). Statistical significance is annotated with letters (measurements with different letters are significant at $P < .050$). Longitudinal tumor volume measurements (E). Interobserver variability was used for the error bar. A large region of necrosis within the tumor is evident on day 12 in panel (A). This animal was euthanized before the final imaging time point on day 15 owing to neurological impairment.

observer variability was calculated from a total of 4 observers, 5 examples, and 5 randomized, repeated measurements.) For each animal and time point, the mean and standard deviation for pH_i and pH_e were calculated from these ROIs (SPSS, IBM Corp., Armonk, NY). All pH errors represent 1 standard deviation of the weighted mean value. The statistical significance across pH_i and pH_e and each day was tested using analysis of variance with Tukey post hoc test and weighted data using the standard deviation of pH measurements. The correlation between pH gradient and tumor volume was tested using Pearson correlation.

Histology

At the experimental endpoint, animals were euthanized and perfused with 4% paraformaldehyde (Sigma Aldrich, Miamisburg, OH). Perfused rat brains were paraffin-embedded and sectioned to 5-μm-thick sections. Then rat brain sections containing tumor were stained with hematoxylin and eosin, Ki67, and HIF1α. These sections were scanned with an AxioImager Z1 Upright Microscope (Carl Zeiss Canada, North York, ON, Canada). Those images were subsequently coregistered with the T2-weighted magnetic resonance images acquired at 3 T using Slicer (Version 4.31, Surgical Planning Laboratory, Brigham & Women's Hospital Boston MA) with a custom software plugin (31).

RESULTS

Of the 7 Wistar rats that were used in this study, 5 survived to the last imaging time point. The other 2 animals were euthanized before the final imaging time point because of neurological impairment related to tumor volume. All animals showed aggressive tumor growth throughout the study, which is an expected feature of the C6 glioma model (19).

Two animals from the cohort were chosen to demonstrate the observed changes in the pH gradient of tumor cells. The first representative animal is shown in Figure 2. This animal did not survive to the final imaging time point but was scanned on days 8 and 12. Rapid tumor growth is evident in Figure 2A and quantified in Figure 2E. At day 12, the dark region within the tumor boundary on the T2-weighted image was indicative of extensive necrosis. Maps of pH_i and pH_e at both imaging time points are provided for comparison in Figure 2B and 2C, and the average pH_i and pH_e for the tumor are provided in Figure 2D. There was a statistically significant difference ($P = .001$) between pH_i and pH_e of the tumor at day 12. There was also a significant increase in pH_i of the tumor ($P = .001$) between days 8 and 12. However, there was no significant change in pH_e of the tumor ($P = .107$). A second representative case is shown in Figure 3. This animal was scanned on days 8, 12, and 15 before sacrifice. This animal also exhibited a rapidly growing tumor as shown in Figure 3A and quantified in Figure 3E. Again, pH_i and pH_e maps of the rat brain are shown in Figure 3, B and C and average pH_i and pH_e of the tumor are shown in Figure 3D. Only at day 12 and 15 was there a statistically significant difference between pH_i ($P = .001$) and pH_e ($P = .002$) within the tumor. Tumor necrosis was not evident with T2-weighted MRI. Increased pH_i within the tumor

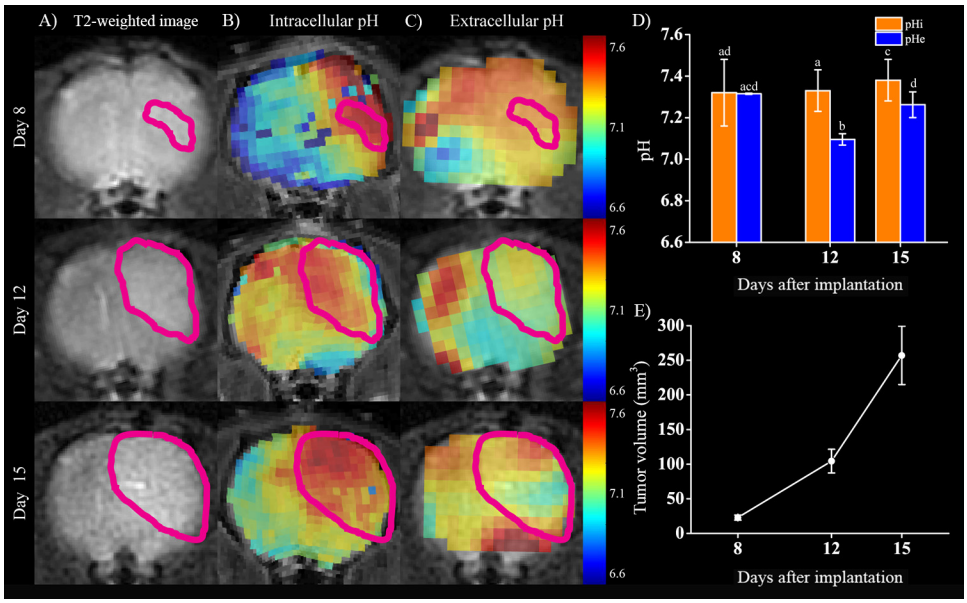

Figure 3. The progression of intra- and extracellular pH of a representative C6 glioma. Panels (A) (B) and (C) present the T2-weighted images, intracellular pH map and extracellular pH map of the rat brain, respectively, at days 8, 12, and 15. Tumors are contoured in magenta. Quantification of changes of intra- and extracellular tumor pH (D). Statistical significance is annotated with letters (measurements with different letters are significant at $P < .050$). Longitudinal tumor volume measurements (E). Interobserver variability was used for the error bar.

was only significant ($P = .001$) at day 15. The pH_e of the tumor was significantly decreased ($P = .001$) at day 12 compared with that at day 8 but increased again by day 15.

Longitudinal changes in average pH gradient and tumor volume of all animals are shown in Figure 4. Figure 4A shows the average pH_i of tumors and contralateral brain on days 8, 12, and 15. Between days, there was no significant difference for measured pH_i within either tumor or contralateral brain tissue; however, tumor pH_i was significantly larger ($P = .001$) than contralateral brain at all days. Similarly, Figure 4B shows the average pH_e of tumors and contralateral brain on days 8, 12, and 15. There was no significant difference detected on day 8 between tumor and contralateral tissue. However, there were significant reductions ($P = .001$) in tumor pH_e on days 12 and 15 and a significant increase ($P = 0.001$) in contralateral brain pH_e on day 15. Significant differences between tumor and contralateral brain pH_e were observed on days 12 and 15 ($P = .001$). Figure 4C illustrates the comparison between pH gradients in tumors and contralateral brain tissue on days 8, 12, and 15. The pH gradient within tumors increased significantly over the 3 imaging time points ($P = .001$). The pH gradient for contralateral brain regions did not change significantly over this period, but it was consistently less than that observed within the tumors. Finally, Figure 4D shows the average tumor volume for days 8, 12, and 15. Tumor volumes significantly increased ($P = 0.001$) between imaging time points.

The association between tumor volume and pH gradient is plotted in Figure 5. Averaging over all animals and time points, there was no significant correlation ($P = .258$). However, when tumors with extensive necrosis were excluded, tumor volume was correlated with pH gradient ($P = .020$) with a Pearson coefficient of 0.715.

Histology for the second representative animal case is shown in Figure 6 with corresponding pH and imaging data. The T2-weighted image showed no clear sign of necrosis; however, necrotic parts of tumor were clearly distinguished from nonnecrotic parts by histology. The whole tumor region showed a relatively high pH_i and low pH_e compared with contralateral brain tissue. Hematoxylin and eosin staining revealed an extremely high density of cells within the tumor compared with normal brain tissue. Further, necrosis was formed within the core of the tumor. HIF-1 showed a higher expression in tumor compared with brain tissue, except within the necrotic region of the brain. Similarly, Ki-67 staining showed greater cellular proliferation in the tumor and no proliferation within the necrotic core and the brain tissue surrounding the tumor.

DISCUSSION

The purpose of this longitudinal study was to map and quantify the change in tumor pH gradient using a rodent model of glioma. To the best of our knowledge, this is the first study to sequentially measure both pH_i and pH_e at multiple time points during tumor progression in an in vivo model. This enabled direct calculation of the cellular pH gradient within the tumor and surrounding tissue. Knowledge of changes in cellular pH gradient in tumors may be important for understanding biological changes in tumors (metabolism, vascularization, and proliferation) and informing on possible treatment strategies (chemo- and radiotherapies) (8, 9).

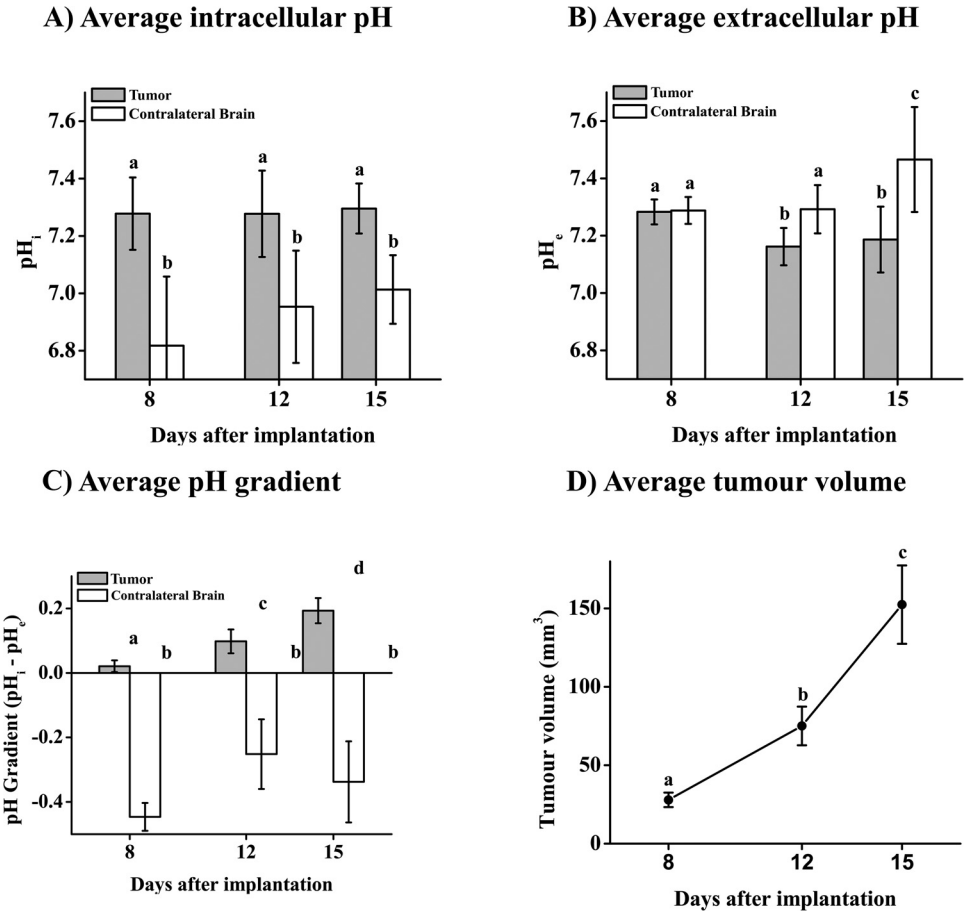

Figure 4. Longitudinal changes in cohort-averaged pH measurements. Panels (A) and (B) show intracellular pH and extracellular pH in tumor and contralateral brain, respectively, measured on days 8, 12, and 15. Panel (C) compares cellular pH gradient between tumor and contralateral brain at those same days. Average gross tumor volume measured from T2-weighted imaging data (D). Interobserver variability was used for the error bar. All statistical significances ($P <$ .050) are annotated with letters.

The C6 rat glioma is a highly proliferating and aggressive solid tumor (19). Tumor volumes increase rapidly as seen in Figures 2–4. Tumor imaging in some animals suggested necrotic cores as shown in Figure 2A, which were also found and confirmed in histology (Figure 6). Changes in tumor volume have been correlated to alterations in tumor pH (32). Hence, dynamic changes in tumor pH were expected commensurate with tumor growth. Owing to rapidly increasing tumor volumes, some animals did not survive to the study endpoint. For animals with rapidly growing tumors, a reversal of pH, as well as a correlation between tumor growth rate and change in tumor pH, was expected.

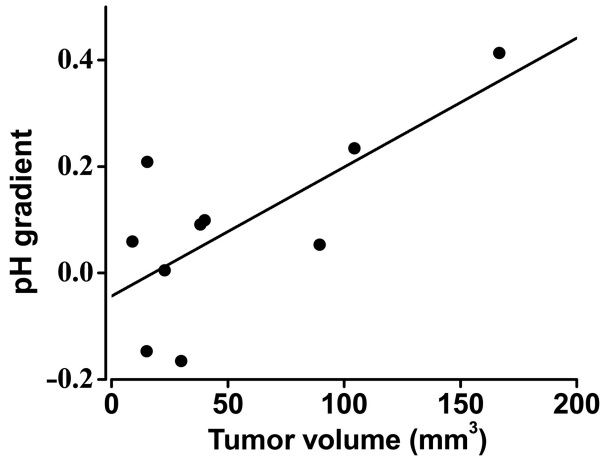

Figure 5. Correlation plot comparing pH gradient and tumor volume. Tumors that did not exhibit necrosis show a significant correlation (green line) between pH gradient and tumor volume (P = .020, Pearson correlation = 0.715)

In general, pH_i and pH_e within tumors and contralateral brain tissue were observed to largely match with what has been previously reported in the literature. As shown in Figure 4A, at day 15, tumor pH_i (7.30 ± 0.09) and tumor pH_e (7.19 ± 0.11) were similar to previously reported values (pH_i = ~7.4 and pH_e = ~6.9) (7-9, 11, 12). Similarly, measurements in contralateral brain tissue (pH_i = 7.01 ± 0.12 and pH_e = 7.46 ± 0.18) were also comparable with previously reported values (pH_i = ~7.2 and pH_e = ~7.4) (7, 9, 10). In addition, these in vivo measurements confirmed the change in pH gradient direction for tumor cells compared with those in contralateral brain tissue. However, it should be noted that the contralateral brain does not represent ideal normal tissue. Elevated intracranial pressure owing to the large tumor burden would likely have an impact on brain tissue pH (33). Although the contralateral brain region did exhibit a consistently negative pH gradient, this region of the brain would likely have been influenced by intracranial hypertension and inflammation (34). Measurements of the pH gradient (pH_i – pH_e) were observed to change sign as early as day 8 in tumors. This was approximately the earliest time point where

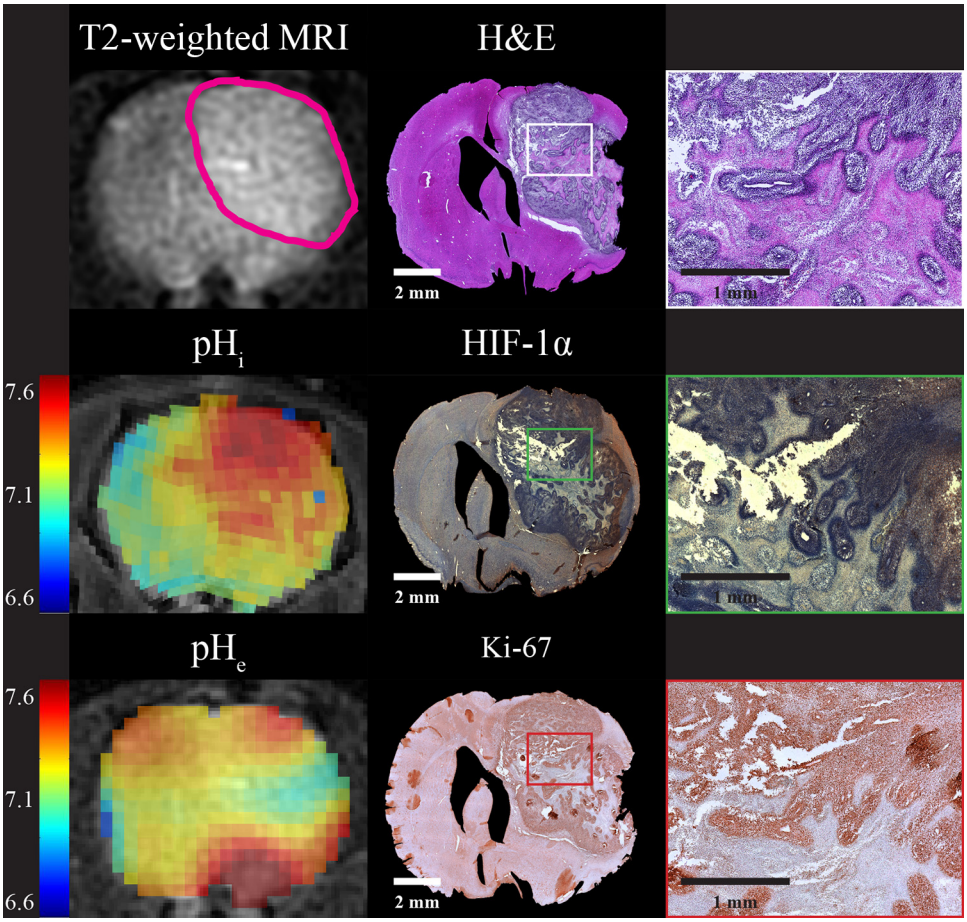

Figure 6. Histology of the second representative animal shown in Figure 3. The first column presents the tumor extent, pH_i, and pH_e within the rodent brain. The tumor margin is outlined in magenta. The second column contains histology including hematoxylin and eosin, HIF-1α, and Ki-67 staining of tumor and brain tissue. The third column of images contains magnified histology of the regions outlined by respective boxes in column 2.

tumor detection and measurement by MRI was reliable for this model.

For each animal, longitudinal measurements of pH_e and pH gradient within the tumor showed a significant decreasing and increasing trend (respectively) as illustrated in Figures 2D and 3D. However, the average pH_i for all tumors did not show any significant trend in time. The trend in tumor pH_e suggests acidification of extracellular space, while the pH_i of tumor cells remains constant during tumor progression. These pH changes are a likely reason for the increase in tumor invasion and proliferation. Conversely, contralateral brain tissue showed no significant change until day 15 when tumors had invaded the other hemisphere of the brain. At this last time point, the contralateral brain tissue was able to maintain pH_i, but pH_e homeostasis was no longer balanced perhaps because of increased edema and reduced perfusion.

These tumors exhibited a large heterogeneity in pH_i and pH_e as shown in Figures 2 and 3. These variations could be due to several biological factors. During tumor progression, tumor metabolism undergoes extensive modification, but these metabolic changes are often not homogenous (35). Furthermore, the decrease in tumor pH_e induces inefficient and nonuniform vascularization (36), leading to further regional variation of pH_i and pH_e (37). Second, at the final time point, some tumors possessed necrotic cores as shown in the histology of Figure 6. This can occur because C6 gliomas often form a necrotic core because of rapid tumor growth and limited supply of nutrients (19). After the tumor cell undergoes necrosis, the integrity of the cellular membrane is jeopardized, and there is no longer a valid distinction between intracellular and extracellular space (38). Therefore, pH_i and pH_e measurements in regions of necrosis would not properly represent tumor pH gradient. In this study, tumor necrosis could not be reliably defined with T2-weighted images. Furthermore, with limited imaging resolution and contrast, it was often difficult to identify necrotic regions before experimental endpoint with histology. Nevertheless, the reversal of pH gradient was observed at all time points when measurements were averaged over the entire tumor volume identified by T2-weighted imaging even though pH measurements were not statistically significant changing across time points.

For individual animals, the change in cellular pH gradient within the tumor was readily apparent. Figure 2 presents a representative animal that died before the final imaging time point. For this case, the tumor grew exceptionally fast, such that the animal suffered significant weight loss and dehydration. Furthermore, rapid tumor growth led to necrosis, which was observed as a hypointense region within the tumor boundary on the T2-weighted image (Figure 2A). This was later confirmed as necrosis by histology. For tumor regions where increasing pH_i and decreasing pH_e was observed, this was likely a consequence of the tumor cells adapting to their microenvironment (15). This tumor also showed heterogeneous pH_i and pH_e throughout the tumor at day 12, particularly in regions where necrosis was suspected compared with the nonnecrotic portion of the tumor. This em-

phasizes the dynamic changes in both tumor pH_i and pH_e. Figure 3 showed another representative case in which the animal survived to the last imaging time point. Unlike the previous case, longitudinal changes in tumor volume, pH_i, and pH_e were less substantial. In this case, pH_e was significantly decreased for day 12 compared with that for day 8, but it significantly increased at day 15. Importantly, this tumor was later confirmed to have a substantial necrotic region by histology (Figure 6), which is likely a factor for the larger range of regional pH measurements. Using only T2-weighted image data, it would be difficult to appreciate the full extent of the heterogeneity of the tumor and its environment. Regional maps of pH_i and pH_e facilitate the visualization of molecular and cellular changes linked to tumor progression in an individual animal.

A modest but significant correlation between tumor volume and pH gradient was observed for this cohort (Figure 5). This correlation was only significant ($P = .001$) when necrotic tumors were excluded. This correlation between tumor volume and pH has been previously reported and these studies suggested a similar conclusion (32, 39). This correlation may explain increased tumor proliferation and invasion owing to changes in tumor microenvironment linked to pH.

The histology in Figure 6 further illustrates the effects of regional tumor pH. Regional differences in pH_i and pH_e compared with those in the contralateral brain corresponded well to the distribution of HIF-1α and Ki-67 measured by histology. In glioma, HIF-1α is upregulated and it further induces metabolic remodeling (40). Ki-67 is a marker for cellular proliferation. Thus, this histology finding shows a potential link between tumor pH gradient, hypoxia, and proliferation. Tumor heterogeneity is also speculated in both the pH maps and histology. The ability to detect and measure tumor proliferation is important for the prognosis of these tumors. In addition, *a priori* knowledge of tumor pH may be useful when used in a strategy of precision medicine to guide selection of an appropriate therapeutic agent on the basis of predicted intracellular uptake from the magnetic resonance-determined pH gradient.

In conclusion, this paper has shown longitudinal mapping of pH_i and pH_e in a rodent model of glioma. This is the first demonstration of noninvasive consecutive in vivo measurement of pH_i and pH_e at multiple time points during tumor progression. This study has shown that within a single tumor, there is a significant regional variation of both pH_i and pH_e within a tumor at a single time point. When these measurements were averaged for all animals at each time point, there was no statistically significant difference across time points. A statistical correlation between tumor volume and pH gradient was observed for nonnecrotic tumors. Highly proliferative regions of the tumor that can be observed by histology were associated with positive pH gradient. Regional molecular information such as pH_i and pH_e provide important information about longitudinal changes in the tumor environment. Knowledge of these changes may ultimately be useful to guide therapeutic choice for treatment of glioma or to assess treatment efficacy. In future work, this glioma model would be useful to monitor and understand the effects of therapy (such as radiotherapy and chemotherapy) and pH-altering drugs (such as dichloroacetic acid) on the tumor pH gradient.

ACKNOWLEDGMENTS

We would like to also recognize the contributions of Yuanxin Chen (histology), Alex Li (acquisition of 9.4 T CEST data), and Miranda Bellyou (animal preparation and handling) toward this research. We also thank Drs. Ferdia A. Gallagher and Albert P. Chen for valuable discussions regarding the hyperpolarized ^{13}C bicarbonate experiments. We gratefully acknowledge funding for this research from the Cancer Imaging Network of Ontario and the Ontario Institute for Cancer Research.

Disclosures: The authors have nothing to disclose.

Conflict of Interest: None reported.

REFERENCES

1. Hanahan D, Weinberg RA. Hallmarks of cancer: the next generation. Cell. 2011; 144:646–674.
2. Vaupel P, Kallinowski F, Okunieff P. Blood flow, oxygen and nutrient supply, and metabolic microenvironment of human tumors: a review. Cancer Res. 1989;49: 6449–6465.
3. Svastová E1, Hulíková A, Rafajová M, Zat'ovicová M, Gibadulinová A, Casini A, Cecchi A, Scozzafava A, Supuran CT, Pastorek J, Pastoreková S. Hypoxia activates the capacity of tumor-associated carbonic anhydrase IX to acidify extracellular pH. FEBS Lett. 2004;577:439–445.
4. Kroemer G, Pouyssegur J. Tumor cell metabolism: cancer's Achilles' heel. Cancer Cell. 2008;13:472–482.
5. Kato Y, Ozawa S, Miyamoto C, Maehata Y, Suzuki A, Maeda T, Baba Y. Acidic extracellular microenvironment and cancer. Cancer Cell Int. 2013;13: 89.
6. Tannock IF, Rotin D. Acid pH in tumors and its potential for therapeutic exploitation. Cancer Res. 1989;49:4373–4384.
7. Webb BA, Chimenti M, Jacobson MP, Barber DL. Dysregulated pH: a perfect storm for cancer progression. Nat Rev Cancer. 2011;11:671–677.
8. Stubbs M, Rodrigues L, Howe FA, Wang J, Jeong KS, Veech RL, Griffiths JR. Metabolic consequences of a reversed pH gradient in rat tumors. Cancer Res. 1994; 54:4011–4016.
9. Gerweck LE, Seetharaman K. Cellular pH gradient in tumor versus normal tissue: potential exploitation for the treatment of cancer. Cancer Res. 1996;56:1194–1198.
10. Swietach P, Vaughan-Jones RD, Harris AL. Regulation of tumor pH and the role of carbonic anhydrase 9. Cancer Metastasis Rev. 2007;26:299–310.
11. Hashim AI, Zhang X, Wojtkowiak JW, Martinez GV, Gillies RJ. Imaging pH and metastasis. NMR Biomed. 2011;24:582–591.
12. Sonveaux P, Vegran F, Schroeder T, Wergin MC, Verrax J, Rabbani ZN, De Saedeleer CJ, Kennedy KM, Diepart C, Jordan BF, Kelley MJ, Gallez B, Wahl ML, Feron O, Dewhirst MW. Targeting lactate-fueled respiration selectively kills hypoxic tumor cells in mice. J Clin Invest. 2008;118:3930–3942.
13. Gatenby RA, Gillies RJ. Why do cancers have high aerobic glycolysis? Nat Rev Cancer. 2004;4:891–899.
14. Brahimi-Horn MC1, Chiche J, Pouysségur J. Hypoxia signalling controls metabolic demand. Curr Opin Cell Biol. 2007;19:223–229.
15. Swietach P, Vaughan-Jones RD, Harris AL, Hulikova A. The chemistry, physiology and pathology of pH in cancer. Philos Trans R Soc Lond B Biol Sci. 2014;369: 20130099.
16. Vander Heiden MG, Cantley LC, Thompson CB. Understanding the Warburg effect: the metabolic requirements of cell proliferation. Science. 2009;324:1029–1033.
17. McVicar N, Li AX, Goncalves DF, Bellyou M, Meakin SO, Prado MA, Bartha R. Quantitative tissue pH measurement during cerebral ischemia using amine and amide concentration-independent detection (AACID) with MRI. J Cereb Blood Flow Metab. 2014;34:690–698.
18. Gallagher FA1, Kettunen MI, Day SE, Hu DE, Ardenkjaer-Larsen JH, Zandt Ri, Jensen PR, Karlsson M, Golman K, Lerche MH, Brindle KM. Magnetic resonance

imaging of pH in vivo using hyperpolarized (13)C-labelled bicarbonate. Nature. 2008;453:940–943.
19. Grobben B, De Deyn PP, Slegers H. Rat C6 glioma as experimental model system for the study of glioblastoma growth and invasion. Cell Tissue Res. 2002; 310:257–270.
20. Zoula S, Rijken PF, Peters JP, Farion R, Van der Sanden BP, Van der Kogel AJ, Décorps M, Rémy C. Pimonidazole binding in C6 rat brain glioma: relation with lipid droplet detection. Br J Cancer. 2003;88:1439–1444.
21. Ward KM, Balaban RS. Determination of pH using water protons and chemical exchange dependent saturation transfer (CEST). Magn Reson Med. 2000;44: 799–802.
22. Zhou J, Blakeley JO, Hua J, Kim M, Laterra J, Pomper MG, van Zijl PC. Practical data acquisition method for human brain tumor amide proton transfer (APT) imaging. Magn Reson Med. 2008;60:842–849.
23. Scholz DJ, Janich MA, Kollisch U, Schulte RF, Ardenkjaer-Larsen JH, Frank A, Haase A1, Schwaiger M6, Menzel MI. Quantified pH imaging with hyperpolarized (13) C-bicarbonate. Magn Reson Med. 2015;73:2274–2282.
24. Martinez-Santiesteban FM, Dang TP, Lim H, Chen AP, Scholl TJ. T1 nuclear magnetic relaxation dispersion of hyperpolarized sodium and cesium hydrogencarbonate-13 C. NMR Biomed. 2017;30.
25. Kim M, Gillen J, Landman BA, Zhou J, van Zijl PC. Water saturation shift referencing (WASSR) for chemical exchange saturation transfer (CEST) experiments. Magn Reson Med. 2009;61:1441–1450.
26. Lim H, Thind K, Martinez-Santiesteban FM, Scholl TJ. Construction and evaluation of a switch-tuned (13) C - (1) H birdcage radiofrequency coil for imaging the metabolism of hyperpolarized (13) C-enriched compounds. J Magn Reson Imaging. 2014;40:1082–1090.
27. Schulte RF, Sperl JI, Weidl E, Menzel MI, Janich MA, Khegai O, Durst M, Ardenkjaer-Larsen JH, Glaser SJ, Haase A, Schwaiger M, Wiesinger F. Saturation-recovery metabolic-exchange rate imaging with hyperpolarized [1-13C] pyruvate using spectral-spatial excitation. Magn Reson Med. 2013;69:1209–1216.
28. Beatty PJ, Nishimura DG, Pauly JM. Rapid gridding reconstruction with a minimal oversampling ratio. IEEE Trans Med Imaging. 2005;24:799–808.
29. Stabenau EK, Heming TA. Determination of the constants of the Henderson-Hasselbalch equation, Alpha-Co2 and Pka, in Sea-Turtle Plasma. J Exp Biol. 1993; 180:311–314.
30. Yushkevich PA, Piven J, Hazlett HC, Smith RG, Ho S, Gee JC, Gerig G. User-guided 3D active contour segmentation of anatomical structures: significantly improved efficiency and reliability. Neuroimage. 2006;31:1116–1128.
31. Gibson E, Crukley C, Gaed M, Gomez JA, Moussa M, Chin JL, Bauman GS, Fenster A, Ward AD. Registration of prostate histology images to ex vivo MR images via strand-shaped fiducials. J Magn Reson Imaging. 2012;36:1402–1412.
32. Engin K, Leeper DB, Cater JR, Thistlethwaite AJ, Tupchong L, McFarlane JD. Extracellular pH distribution in human tumours. Int J Hyperthermia. 1995;11:211–216.
33. Stocchetti N, Maas AI. Traumatic intracranial hypertension. N Engl J Med. 2014; 370:2121–2130.
34. Kaal EC, Vecht CJ. The management of brain edema in brain tumors. Curr Opin Oncol. 2004;16:593–600.
35. Phan LM, Yeung SC, Lee MH. Cancer metabolic reprogramming: importance, main features, and potentials for precise targeted anti-cancer therapies. Cancer Biol Med. 2014;11:1–19.
36. Marusyk A, Almendro V, Polyak K. Intra-tumour heterogeneity: a looking glass for cancer? Nat Rev Cancer. 2012;12:323–334.
37. Wike-Hooley JL, Haveman J, Reinhold HS. The relevance of tumour pH to the treatment of malignant disease. Radiother Oncol. 1984;2:343–366.
38. Raza SM, Lang FF, Aggarwal BB, Fuller GN, Wildrick DM, Sawaya R. Necrosis and glioblastoma: a friend or a foe? A review and a hypothesis. Neurosurgery. 2002;51:2–12; discussion 12-3.
39. Estrella V, Chen T, Lloyd M, Wojtkowiak J, Cornnell HH, Ibrahim-Hashim A, Bailey K, Balagurunathan Y, Rothberg JM, Sloane BF, Johnson J, Gatenby RA, Gillies RJ. Acidity generated by the tumor microenvironment drives local invasion. Cancer Res. 2013;73:1524–1535.
40. Strickland M, Stoll EA. Metabolic reprogramming in glioma. Front Cell Dev Biol. 2017;5:43.